RAR-β is downregulated in HCC & cirrhosis and its expression inhibits myosin-driven activation and durotaxis in hepatic stellate cells

Ernesto Cortes[1*], Dariusz Lachowski[1*], Alistair Rice[1*], Antonios Chronopoulos[1], Benjamin Robinson[1], Stephen Thorpe[2], David A Lee[2], Lucia A Possamai, Haiyun Wang[3], David J Pinato[4§], and Armando E. del Río Hernández[1§]
[1]Cellular and Molecular Biomechanics Laboratory, Department of Bioengineering, Imperial College London, London SW7 2AZ, United Kingdom
[2]School of Engineering and Materials Science, Queen Mary University of London, London E1 4NS, United Kingdom
[3]Division of Integrative Systems Medicine and Digestive Disease, Imperial College London, London W12 0HS, United Kingdom
[4]Department of Surgery and Cancer, Hammersmith Hospital Campus, Imperial College London, London W12 0HS, United Kingdom
[5]School of Life Sciences and Technology, Tongji University, Shanghai 200092, China

[§]Corresponding authors:
Armando E. del Río Hernández, PhD
Cellular and Molecular Biomechanics Laboratory
Department of Bioengineering
Imperial College London
London SW7 2AZ
United Kingdom
email: a.del-rio-hernandez@imperial.ac.uk

David J Pinato, MD MRCP MRes PhD
Department of Surgery and Cancer Hammersmith Hospital Campus,
Imperial College London,
London W12 0HS,
United Kingdom
Email: david.pinato@imperial.ac.uk

Key words: mechanotransduction, myosin light chain 2, retinoic acid receptor beta, ATRA, hepatic stellate cells
Word count: 5866
Number of figures: 8
Conflict of interest
The authors declare no conflict of interest
*equal contribution
Abbreviations
HCC – Hepatocellular carcinoma
ECM – Extracellular matrix
NAFLD – Non-alcoholic fatty liver disease

HSCs – Hepatic stellate cells
PDAC – Pancreatic ductal adenocarcinoma
PSCs – Pancreatic Stellate Cells
CAFs – Cancer associated fibroblasts
MLC-2 – Myosin light chain 2
RAR-β – Retinoic acid receptor β
ATRA – All trans retinoic acid
TMA – Tissue microarray
H&E – Hematoxylin and eosin
PBS – Phosphate buffered saline
ROI – Region of interest
α-SMA – α-smooth muscle actin
pMLC-2 – phosphorylated myosin light chain 2
AFM – atomic force microscopy

Financial Support
This work was supported by the European Research Council (Grant Agreement 282051).

Abstract
Hepatic stellate cells (HSCs) are essential perisinusoidal cells in the healthy and diseased liver. HSCs modulate extracellular matrix (ECM) homeostasis when quiescent, but in liver fibrosis, HSCs become activated and promote excess deposition of ECM molecules and tissue stiffening via force generation and mechanosensing. In hepatocellular carcinoma (HCC), activated HSCs infiltrate the stroma and migrate to the tumor core to facilitate paracrine signalling with cancer cells. Since the function of HSCs is known to be modulated by retinoids, we investigated the expression profile of retinoic acid receptor beta (RAR-β) in cirrhotic and HCC patients, as well as the effects of RAR-β activation in HSCs. We found that RAR-β expression is significantly reduced in cirrhotic and HCC tissues. Using a comprehensive set of biophysical methods combined with cellular and molecular biology, we have elucidated the biomechanical mechanism by which all trans-retinoic acid (ATRA) promotes HSC deactivation via RAR-β-dependent transcriptional downregulation of myosin light chain 2 (MLC-2) expression. Furthermore, this also abrogated mechanically driven migration towards stiffer substrates. *Conclusion:* Targeting mechanotransduction in HSCs at the transcriptional level may offer new therapeutic options for a range of liver diseases.

Hepatocellular carcinoma (HCC) is the most relevant form of liver cancer and the second most deadly cancer globally (1). This disease develops most commonly in individuals with sustained liver fibrosis or cirrhosis, following chronic inflammation of the liver (2). The development of fibrosis involves the deposition of high levels of extracellular matrix (ECM) proteins and increased tissue tension, which together produce a stiff desmoplasia that promotes progression to cirrhosis (3, 4). Non-alcoholic fatty liver disease (NAFLD), a growing worldwide epidemic (5), also involves liver fibrosis in a large number of cases (6). The role of fibrosis in the early and late stages of liver diseases highlights the urgent need to find therapies that target this desmoplastic reaction.

Hepatic stellate cells (HSCs) are perisinusoidal cells, residing in the liver (7), with roles in retinoid storage (8) and force-mediated maintenance of the extracellular matrix (9). In HCC, HSCs transition from a quiescent to a contractile activated state, and promote tumor development through production of a fibrotic stroma (10). HSCs also engage in cross-talk with cancer cells in positive-feedback loops that maintain the activated phenotype of HSCs as well as promoting the growth of cancer cells (11). Furthermore, the elevated deposition of fibronectin from activated HSCs drives the formation of the pre-metastatic niche that precedes liver colonization by pancreatic ductal adenocarcinoma (PDAC) cells (12).

HSCs are generated in the bone marrow along with pancreatic stellate cells (PSCs) (13), and share many equivalent functions with PSCs, such as storage of vitamin A droplets and ECM homeostasis. When activated, both cell types lose their vitamin A droplets and show high levels of stromal remodelling through their contractile myofibroblast-like phenotype (14). Cancer associated fibroblasts (CAFs), like activated HSCs and PSCs, are myofibroblast-like cells and correspondingly drive tumor progression through restructuring of the tumor microenvironment (15). The similarity between these cell types highlights the importance of cell mechanics in tumor malignancy, and suggests that targeting the mechanical phenotype of these cells would be pertinent.

Activated HSCs, activated PSCs, and CAFs perpetuate fibrosis and a tumor-permissive microenvironment through multiple positive-feedback loops that increase the active population of these cells. The actomyosin-dependent mechanical loop remodels and stiffens the ECM to a fibrotic state, and then responds to external rigidity by increasing cell contractility though myosin light chain 2 (MLC-2) regulation and inducing pro-fibrotic signalling pathways (9, 15-17). In addition, HSCs have been shown to infiltrate into the tumor stroma and localise around the cancer cells, facilitating paracrine signalling (18). Durotaxis, the process of directed migration based on substrate rigidity, has been observed in HSCs and is suggested to lead to accumulation of HSCs and further potentiation of fibrosis as migrating HSCs become activated by the stiff environment (19).

The retinoic acid receptor family is known to modulate the function of HSCs, though the molecular mechanisms behind this regulation are not well understood. Elucidating the molecular events underlying HSC activation holds the key to blocking progression of early and advanced liver diseases. Here we show that expression of RAR-β is significantly downregulated in HCC and cirrhotic patients in comparison with healthy individuals. We observed that ATRA (all trans-retinoic acid) induces the RAR-β-mediated negative transcriptional regulation of MLC-2, and consequently reduces force generation and mechanosensing. These processes sustain the stiff microenvironment needed for the activated phenotype in HSCs. Furthermore, deactivated HSCs have an impaired ability to remodel the matrix and do not display directed migration toward stiffer substrates.

Experimental Procedures

Tissues microarrays

Tissue microarray (TMA) blocks were constructed as previously described (20) using 20 archival paraffin-embedded HCC tissue blocks and 10 healthy controls retrieved from the Imperial College London Tissue Bank (Ethical Approval nr.R15058). All experiments were performed in accordance with the Imperial College guidelines and regulations. All experimental protocols have been approved by the Research Ethics Committee Wales approval 12/WA/0196, license number 12275. Written consent was obtained from all subjects. A consultant histopathologist reviewed all the materials prior to inclusion on freshly cut hematoxylin & eosin (H&E) slides. We constructed TMA blocks using an MTA-1 Microarrayer (Mitogen, UK) following H&E-slide guided microdissection of target tumor and surrounding non-tumorous areas. We obtained triplicates of 1 mm cores from separate central and peripheral areas of tumor and matching surrounding liver. Adequate sampling of target tissues was confirmed on a freshly cut H&E section from the recipient TMA block before downstream analysis. For quantification of the levels of RAR-b, MLC-2, and pMLC-2 in human liver tissues from healthy, cirrhosis, and HCC (T1, T2, T3, and T4), the TMAs were obtained from Biomax (Catalog number: BC03117).

Murine fibrosis model

All research using live animals was approved by local ethics committees (Imperial College Central Animal Welfare Ethical Review Board (AWERB)) and was carried out under Home Office supervision in accordance with the European Directive 2010/63/EU. All animals received humane care according to the criteria outlined in the "Guide for the Care and Use of Laboratory Animals" prepared by the National Academy of Sciences and published by the National Institutes of Health (NIH publication 86-23 revised 1985) Mice were housed in specific pathogen free conditions in individually ventilated cages (Techniplast UK Ltd). The environment was controlled with a 12 hour light/dark cycle, ambient temperature of 21°C (+/- 2°C) and humidity of 55% (+/-10%). Mice had access to irradiated diet (Special Diet Services UK) and water (25ppm chlorine) ad libitum. Five male C57BL/6 mice, aged 8-12 weeks, were dosed twice weekly for six weeks with 0.4µl/g CCl_4 diluted 1 in 3 in olive oil, administered via the intraperitoneal route. Three male age and strain-matched co-housed 'vehicle only' control mice were dosed to the same regimen with the same by weight volume of olive oil. Mice were culled 72 hours following the last injection of CCl_4. To validate the induction of fibrosis, Sirius Red staining was performed (by the Department of Pathology, St Mary's Hospital Imperial College London). The collagen proportionate area (CPA) was calculated by quantification of the area of collagen (Sirius red stained tissue) as a proportion of the total tissue area using Image J. Eight representative fields at x10 magnification were assessed for each mouse.

Cell culture and antibodies

Primary, culture-activated human hepatic stellate cells (HSCs), passage 3-6, HHStec 5300; ScienCell, Carlsbad, CA, USA) were cultured in phenol red medium (DMEM-F12 HAM, Sigma Aldrich, D6434) supplemented with 10% Foetal Bovine Serum (Gibco, 10500-064), 1% Penicillin/Streptomycin (Sigma Aldrich, P4333), and 1% Fungizone R Amhotenicin (Gibco, 15290-026). HSCs were treated with 1 µM ATRA dissolved in absolute ethanol (Fisher, E/0650DF/17) for 10 days. Control HSCs were culture with an equivalent amount of 0.1% ethanol in media as vehicle control. Medium for both control and ATRA treated HSCs was changed every 24 h and changing of media was performed in subdued light. Both control and ATRA treated HSCs were incubated with phenol red culture medium supplemented with 2% Foetal Bovine Serum. HSCs were exposed to 1 µM of agonist for 72 h. RAR-β agonist (cd2314, Tocris, 3824). RAR-β antagonist (cd2665, Tocris, 3800) used at 1 µM. All cells were tested

for mycoplasma contamination. Antibodies: RAR-β receptor (Abcam, ab53161), MLC-2 (Millipore, MABT180, WB 1/100 and IF 1/200), pMLC-2 /Thr18/Ser19 (Cell Signalling, 3674, WB 1/100, IF 1/200), Anti-Mouse HRP (Invitrogen, 626580, 1/2,000), Anti-Rabbit HRP (Abcam, ab137914, 1/2,000), and Anti-Mouse 488 (Invitrogen, A11029, 1/400).

RT–PCR

Total RNA was extracted using the RNeasy Mini kit (Qiagen, 74104) and 1 µg of total RNA was reverse-transcribed using the High-Capacity RNA-to-cDNA kit (Applied Biosystems, 4387406) according to the manufacturer's instructions. qPCR was performed using the SYBR Green PCR Master Mix (Applied Biosystems, 4309155) with 100 ng cDNA input in 20 µl reaction volume. GAPDH expression level was used for normalization as a housekeeping gene. The primer sequences for were as follows: GAPDH: forward-5′-ACAGTTGCCATGTAGACC-3′, reverse-5′-TTTTTGGTTGAGCACAGG-3′; RAR-β: forward 5'- AATAAAGTCACCAGGAATCG -3' and reverse, 5'-CAGATTCTTTGGACATTCCC -3'; MLC-2: forward, 5′-ATCCACCTCCATCTTCTT-3′ and reverse, 5′-AATACACGACCTCCTGTT-3′. All primers were used at 300 nM final concentration. The relative gene expression was analysed by comparative 2−ΔΔct method.

Analysis of RAR-β gene expression

The RNA-seq data of 371 HCC patients and 50 normal samples were obtained from TCGA project (TCGA data version: 2016_01_28). The abundance of each gene was quantified as RSEM value, which was evaluated by a statistical method RSEM (RNA-Seq by Expectation Maximization). RSEM uses a generative model of RNA-seq reads and the EM algorithm, taking read mapping uncertainty into account and achieving the most accurate abundance estimates (21). The statistical analysis of differentially expressed genes was performed using DESeq2 (22) package of Bioconductor in R statistical software (http://www.bioconductor.org/packages/release/bioc/html/DESeq2.html).

Immunofluorescence staining

Cell immunofluorescence staining was done on coverslips coated with 10 µg ml^{-1} fibronectin (Gibco, phe0023). Following pertinent treatment, cells were fixed with 4% paraformaldehyde (Sigma, P6148) in D-PBS (Sigma, D8537) for 10 min, and then blocked and permeabilized with 0.2% BSA, 0.1%Triton (Sigma, T8787) in PBS for 30 min. After blocking, cells were incubated with primary antibodies prepared in blocking solution for 1 h at room temperature in a humidified chamber. Then, cells were washed in D-PBS and incubated with Alexa Fluor 488-conjugated secondary antibodies and Phalloidin (Invitrogen, A22283, 1/1,000 dilution) prepared in PBS for 30 min at room temperature. Finally, coverslips were washed in PBS and mounted in mounting reagent with 4,6-diamidino-2-phenylindole (Invitrogen, P36931). Immunofluorescent images were taken with Nikon Ti-e Inverted Microscope (Nikon, Kingston-upon-Thames, United Kingdom) with NIS elements software.

Traction forces using elastic pillars

Pillar arrays were created by mixing polydimethylsiloxane (PDMS) and a curing agent (Sylgard 184) in a 10:1 ratio, and pouring this mixture into a pillar mould with holes of 5 µm depth. This was incubated at 70 ºC for 12 hours for the PDMS to set. Once separated from the mould, PDMS pillars were coated with fibronectin (10 µl/mL PBS) for 1.5 hr at 37 ºC. The solution surrounding the pillars was replaced with PBS for washing, and then replaced by cell medium. Cells were trypsinized and resuspended in culture medium and seeded onto the pillars, then incubated for 1 hr at 37 degrees 5% CO_2 before transfer to a Nikon Ti-e microscope in a 37 ºC temperature-controlled chamber. Videos of different cells were taken at 1 frame per

second for 60 seconds, and each pillar mould was imaged for a maximum time of 30 mins to ensure cell viability. The position of each pillar in the time-lapse videos was tracked using a custom MATLAB program to track the centre of a point spread function of the intensity of the pillars across all frames. By selecting a location free of cells, tracking of a small set of pillars allowed a measurement of the stage drift to be obtained and corrected for the data set. The time-dependent displacement of a given pillar was obtained by subtracting the initial position of the pillar (zero force) from the position in each frame. Traction forces were obtained by multiplying the pillar displacements by the pillar stiffness, determined from pillar height. The maxima for each pillar were found to obtain the average peak force across the cell.

Cell mechanosensing

HSCs (control or ATRA treated) were incubated with 4.5 µm fibronectin-coated magnetic beads coated for 30 minutes and then subjected to a pulsatile force regimen applied with magnetic tweezers, consisting of a 3 s, 1 nN pulse of force, followed by a 4 s period of rest, repeated for 12 total pulses over a 100 s time course. The ability of the cells to sense and respond to the applied tension was examined from the rapid cell stiffening response evident by the progressive decrease in amplitude of the bead movement (n=16 for control and n=16 for ATRA).

3D ECM remodelling assay

HSCs (control or ATRA treated), were embedded in Collagen-I (BD Bioscences, 354249, stock concentration 9.37 mg ml−1) and Matrigel (BD Bioscences, 354234, stock concentration 9 mg ml^{-1}) mixture gels. The gels were prepared with one part 10× DMEM (Sigma, D2429) and one part FBS (Gibco, 10500), yielding to a final concentration of 4.5 mg ml^{-1} Collagen-I and 2 mg ml^{-1} Matrigel. The gel mixture was neutralized with 1 M NaOH (Sigma, S8045), then 5×10^5 cells were embedded in gels in culture media. A measure of 80 µl gel volume was added per well of a 96-well plate, which was pre-treated with 2% BSA (Sigma, A8022) for 1 h, washed with PBS and air dried for 10 minutes. Gels were set 1 h at 37 °C, and then incubated with culture media at 37 °C. After incubation, gels were blocked with 1% BSA–0.1% Triton X-100 in PBS for 1 h.

MLC-2 rescue and functional assays

To re-introduce MLC-2 expression in ATRA-treated HCSs; HSCs were treated with 1 µM ATRA for 10 days, and then transfected with 2 µg MLC-2 plasmid, (pEGFP-MRLC1, a gift from Tom Egelhoff, Addgene plasmid #35680) for 4 h using JetPRIME reagent (1:3 DNA:jetPRIME ratio (w/v)) and JetPRIME buffer (Polyplus, 114-15). During transfection, cells were cultured in 2 ml media without ATRA to exclude the possibility of it affecting the transfection efficiency. After transfection, culture media was changed with 2 ml media containing ATRA. Mock transfection was done using JetPRIME reagent and buffer only (i.e. without DNA) and the cells were otherwise treated the same way as the transfection group. Functional assays were done 48 h after transfection. To study the effect of MLC-2 overexpression on ECM remodelling, MLC-2 overexpressing ATRA-treated PSCs and mock transfection group were trypsinised and 500,000 cells were embedded in 80 µl Collagen-I Matrigel mixture gels (4.5 and 2 mg ml−1 final concentration, respectively). After 1 h incubation at 37 °C on 2% BSA-treated wells of 96-well plate, gels were covered with ATRA-containing media and left to be remodelled at 37 °C. Gel contraction was calculated as % reduction in the gel surface area.

Quantification and analysis of durotaxis on polyacrylamide hydrogels

Durotaxis of cells was analysed with a Nikon Ti-Eclipse microscope using a 20x objective. After cell seeding onto dual-rigidity hydrogels, samples were transferred to microscope culture chamber (37°C, 5% CO2) and gently submerged in 5 mL of growth media. The rigidity boundary was identified through yellow-green fluorescence of FluoSpheres. Regions of interest (ROI) across the sample were stitched together using NIS elements software to generate a representative image of the hydrogel surface. x- and y-axes were used to define these ROI within the 'soft', 'stiff' and 'rigidity gradient' regions of the hydrogel, whilst the z-axis was used to focus the camera onto the surface plane of the gel. A period of 1-2 hours was set to allow cells to fully attach to gel surface before time-lapse phase contrast images were taken every 10 minutes for 5.5 hours within each designated ROI. Coordinates and distances of cell movement were calculated using the Fiji "Manual Tracking" plugin.

Atomic force microscopy

Measurements of cell compliance were conducted on a Nanowizard-1 (JPK Instruments, Berlin, Germany) atomic force microscope (AFM) operating in force spectroscopy mode mounted on an inverted optical microscope (IX-81; Olympus, Tokyo, Japan). Atomic force microscopy pyramidal cantilevers (MLCT; Bruker, Camarillo, CA, USA) with a spring constant of 0.03 N/m were used with a 15 μm diameter polystyrene bead attached. Before conducting measurements, cantilever sensitivity was calculated by measuring the force–distance slope in the AFM software on an empty petri dish region. For each cell analysed, force curves were acquired at an approach speed of 5 μm/s and a maximum set point of 1 V. The force–distance curves were used to calculate elastic moduli in the AFM software through the application of the Hertz contact model (23).

Statistical analysis

All statistical analyses were conducted with the Prism graphical software (GraphPad, Software). Data were generated from multiple repeats of different biological experiments to obtain the mean values and s.e.m displayed throughout. P values have been obtained through t-tests on paired or unpaired samples with parametric tests used for data with a normal distribution and non-parametric tests conducted via the Mann–Whitney test where data had a skewed distribution. Significance for the t-tests was set at $P<0.05$ where graphs show significance through symbols (*$P<0.05$; **$P<0.01$; ***$P<0.001$).

Results

RAR-β is decreased in cirrhotic and HCC human liver tissues

To investigate whether RAR-β is differentially expressed in hepatic tissues, we used tissue microarrays and immunofluorescence of human liver tissues from healthy individuals and patients with cirrhosis. Activated HSCs *in vitro* have been shown to have reduced expression of RAR-β compared to their quiescent state (24) and HSCs isolated from cholestatic liver fibrosis also show a diminished RAR-β expression (25).

We identified activated HSCs and other myofibroblasts in the tissue section using positive staining of α-smooth muscle actin (α-SMA), a widely accepted marker for activated HSCs (7). We observed that RAR-β was abundantly expressed in healthy tissue, which was also characterised by very low or neglectable abundance of activated HSCs. In cirrhotic liver, RAR-β was greatly reduced in areas where activated HSCs were present (Fig. 1A and Supplementary Figure 1), in concurrence with the known reduction of RAR-β expression in activated HSCs (24). The overall expression of RAR-β across the tissue was 70% lower in cirrhotic tissue compared to healthy tissue (Fig. 1B).

Solid tumors in multiple organs are characterised by a decrease in RAR-β expression (26). We analysed the gene expression of this receptor using samples of 371 HCC patients and 50 healthy individuals from the cancer genome atlas (TCGA) dataset and observed that the expression of RAR-β in HCC patients was significantly lower than in normal samples (p=7.11e-06) (Fig. 1C). This trend correlates with our immunofluorescence results, which indicates that the loss of RAR-β expression occurs primarily in the activated HSC population, and reveals that like multiple other tumors, loss of RAR-β expression may be associated with malignancy in the liver.

ATRA induces the expression of RAR-β and negatively regulates MLC-2 *in vitro*

ATRA is an active vitamin A metabolite and a known exclusive agonist of RARs, including RAR-β (27). Vitamin A has been shown to positively regulate RAR-β expression in rat maternal tissues (28). HSCs are known to express all isoforms of the RAR family (α, β and γ), each of which are differentially responsive to various retinoids (24). We treated HSCs with 1 μM ATRA for 10 days, a concentration and time comparable to those in previous studies on similar cells (29-31). The mRNA expression of RAR-β was significantly increased in ATRA-treated HSCs compared to control (Fig. 1D). RAR-β expression was also upregulated at the protein level in HSCs after ATRA treatment (Fig. 1 E, F and Supplementary Figure 2). Collectively, this indicates an increase in RAR-β expression at both the gene and protein levels in response to ATRA.

It has been observed that tissue tension promotes chronic HSC activation (9, 32). Thus, we investigated whether RAR-β activation in HSCs affected the expression of myosin light chain-2 (MLC-2), a key regulatory protein in cytoskeletal contractility (33). Using qPCR, we observed that treatment of HSCs with a RAR-β agonist (cd2314) for 72 hours induced a significant decrease in MLC-2 mRNA expression, a reduction also observed with the 10-day ATRA treatment. Combining ATRA treatment with a RAR-β antagonist (cd2665) prevented the effect of ATRA, with control levels of MLC-2 mRNA expression observed (Fig. 2A). This suggests that ATRA downregulates MLC-2 levels through RAR-β activation.

Immunofluorescence staining was also used to assess protein levels of MLC-2 and its phosphorylated active form, pMLC-2. Both ATRA treatment for 10 days and RAR-β agonist treatment for 72 hours were observed to reduce the protein levels of total MLC-2, and proportionally, levels of the active form of MLC-2 (pMLC-2) (Fig. 2 B, C). Compared to the control condition, ATRA + RAR-β antagonist treatment for 10 days, and RAR-β agonist treatment for 72 hours after RAR-β was knocked down using siRNA, did not show significantly different levels of expression of either MLC-2 or pMLC-2.

We also studied the effect of ATRA treatment for 72 h in the MLC-2 and pMLC-2 levels of HSCs. We observed a significant inhibition in the levels of both MLC-2 and pMLC-2 using immunofluorescence and western blot. ATRA exposure for 72 h after HSCs were treated with siRNA against RAR-β did not show significantly different levels of expression of MLC-2 and pMLC-2 compared to control (Supplementary Figure 3). Taken together, these results confirm the RAR-β dependent negative regulation of MLC-2 expression in HSCs via RAR-β.

MLC-2 is upregulated in cirrhosis and HCC

In order to investigate further the relationship between RAR-β and MLC-2 in fibrosis, we assessed protein levels of RAR-β and MLC-2 in healthy and fibrotic mouse models. We used C57BL/6 mice, aged 8-12 weeks, and randomized them in two groups. One group was injected with CCl_4 (via intraperitonial injection) for six weeks to induce fibrosis and the other was

administered olive oil as vehicle control. CCl_4 induced fibrosis is a well validated model of murine fibrosis (34). To validate the induction of fibrosis, Sirius Red staining was performed. The collagen proportionate areas increased around four times in tissues from CCl_4 treated mice compared to vehicle control (Supplementary Fig 4). We observed a significant reduction in the expression of RAR-β, and an overall two-fold increase in MLC-2 expression in fibrotic tissues compared to vehicle control. We used α-SMA staining to identify HSCs (myofibroblast phenotype) and observed neglectable levels of α-SMA in control tissues but substantial expression in fibrotic tissues, where the α-SMA positive stained areas showed almost no expression of RAR-β. In stark contrast, MLC-2 staining co-localized with the α-SMA positive stained areas in CCl_4 treated fibrotic tissues. In control tissues, MLC-2 was expressed at very low levels and always in α-SMA positive cells (Fig 2 D).

We then used human tissues from healthy, cirrhotic and HCC livers and quantified the levels of expression of RAR-β, MLC-2, and pMLC-2. Staining with α-SMA identified HSCs and other myofibroblast-like cells. In healthy tissues we observed very little expression of α-SMA, but substantial expression of RAR-β, most likely in healthy hepatocytes. Cirrhotic and HCC tissues showed large α-SMA positive areas that co-localized with MLC-2 and pMLC-2 but not with RAR-β expression (Fig. 3A). Overall the RAR-β expression was gradually and significantly decreased from healthy to cirrhotic to HCC tissues, while MLC-2 and pMLC-2 expression were upregulated two-fold from healthy to HCC tissues (Fig. 3B). Based on TNM staging criteria (7^{TH} Edition)(35), we then classified the HCC specimens according to their T stage in two groups: T1/T2 (early stage) and T3/T4 (advanced stage). When we compared T3/T4 versus T1/T2 group we found a 20% decrease in RAR-β expression associated with a stage-dependant 30% increase in MLC-2 levels.

In order to conduct functional experiments in a physiological relevant system, we cultured HSCs on 12 kPa polyacrylamide (PAA) gels, fabricated using a previously reported protocol (19). The use of these gels recapitulates a biomechanical environment close to fibrotic liver tissue (36). RAR-β was expressed in control HSCs at a modest level, but the expression increased by 50% following ATRA treatment for 72 h. Notably, RAR-β showed a very high nuclear localization in ATRA treated HSCs compared to control HSCs. ATRA treatment significantly decreased MLC-2 levels in HSCs, but the levels comparable to control HSCs were observed following ATRA treatment in the presence of siRNA against RAR-β (Fig 3D,E). Taken together, these results indicate that MLC-2 and pMLC-2 are upregulated in cirrhotic and HCC tissues and strongly suggest that ATRA treatment negatively regulates MLC-2 via RAR-β *in vivo*.

ATRA inhibits force generation and mechanosensing in HSCs

Cytoskeletal rearrangement and increased actomyosin contractility are required for the maintenance of the activated phenotype in HSCs (37). Myofibroblasts, which bear phenotypic resemblance to activated HSCs, also require high cytoskeletal contractility for their function (17). This highly mechanoresponsive and contractile phenotype of HSCs is adaptive in a wound-healing context but can promote fibrosis in a disease context (32).

We used elastic pillars to assess the effect of ATRA treatment on force generation in HSCs. Polydimethylsiloxane pillars were coated with fibronectin to facilitate cell attachment and the deflection of each pillar was monitored during the process of cell spreading. The traction force

per pillar was calculated using its deflection and the known Young's modulus of the pillar array. ATRA-treated HSCs (10 days) were observed to generate significantly reduced traction forces compared to control HSCs but this inhibition was lost when ATRA was combined with RAR-β antagonist. Similarly, 72 hours RAR-β agonist treatment significantly reduced force generation but the effect was rescued when the treatment was performed after siRNA mediated knock down of RAR-β (Fig. 4A, B). 72 hour ATRA treatment also led to significantly reduced force generation, whereas ATRA treatment combined with siRNA against RAR-β led to generation of forces similar to control (Supplementary Fig. 5)

Cytoskeletal stiffness is associated with the rheological properties of cells and their ability to generate forces (38, 39). HSC activation requires reorganisation of the actin cytoskeleton, and cytoskeletal disrupting drugs, which are known to reduce the Young's modulus of cells (40), inhibit the activated phenotype (41). We used atomic force microscopy (AFM) indentation of individual cells to study HSC elasticity and observed a reduced Young's modulus in 10-day ATRA-treated HSCs (softer HSCs), implying a reduced cytoskeletal tension. This effect was reverted when ATRA was supplied simultaneously with the RAR-β antagonist. We also observed that RAR-β agonist (72 hour treatment) reduced the Young's modulus, but not after HSCs were treated with siRNA against RAR-β (Fig. 4C). Similarly, ATRA treatment for 72 hours led to cell softening, but no difference to control was seen when the treatment followed transfection of HSCs using siRNA against RAR-β (Supplementary Fig. 5).

The capacity of cells to apply forces on their substrates correlates with their ability to remodel the underlying matrix (17). To further investigate the effect of ATRA on the ability of HSCs to remodel the ECM, we embedded Matrigel-collagen gels with HSCs and allowed them to contract the gels. 10-day ATRA-treated HSCs showed a significantly reduced capacity to contract the gels, comparable to treatment of HSCs with the myosin II ATPase inhibitor Y27632 (Fig. 4 D). Treatment of cells with both ATRA and Y27632 did not further reduce gel contraction, supporting the fact that ATRA exerts its effects through reduction of actomyosin contraction. Additionally, the ability to contract the gels was rescued by transfecting ATRA-treated HSCs with a plasmid to promote MLC-2 overexpression (Supplementary Fig. 6).

Mechanosensing ECM rigidity also relies on cytoskeletal rearrangement and actomyosin contractility (42). Mechanosensing was assessed using magnetic tweezers microrheology, in which fibronectin-coated magnetic beads are attached to the cell of interest via integrin receptors and undergo 12 consecutive pulses of equal force. Mechanoresponsive cells reduce the amplitude of these pulses (Fig. 4 E) as force application to a localised cell area of integrins triggers an adaptive reinforcement, requiring cytoskeletal remodelling through the RhoA-ROCK-MLC-2 signalling axis (42). Ostensibly, this behaviour allows a cell to regulate its cytoskeletal stiffness in response to its mechanical environment. We observed that control HSCs responded to the external mechanical stimulus applied by the bead by showing a significant cytoskeletal stiffening, as the 12^{th} pulse was significantly smaller than the 1^{st} pulse, whereas 10-day ATRA-treated cells did not show this significant reduction (Fig. 4F). This reveals that ATRA treatment impairs the ability of HSCs to respond to external forces, i.e. mechanosensing.

ATRA induces mechanical quiescence in HSCs

Force generation and mechanosensing of ECM rigidity are essential to promote the activated phenotype in myofibroblasts (43). The activation of stellate cells is characterised by a lack of the cytoplasmic lipid droplets, which are present in the quiescent state, as well as increased

expression of α-SMA and vimentin (44). α-SMA contributes to mechanical tension within myofibroblasts (39) and the intermediate filament component vimentin can mediate cytoskeletal organisation and focal adhesion maturation (45).

Immunofluorescence staining of α-SMA and vimentin indicated higher levels of these proteins in control HSCs compared to 10-day ATRA-treated HSCs. The effect of ATRA was lost in the presence of the RAR-β antagonist. The treatment of HSCs with RAR-β agonist (72 hours) also decreased expression of α-SMA and vimentin, and this effect was not observed when the treatment was performed after transfecting HSCs with siRNA RAR-β (Fig. 5A, B). ATRA treatment for 72 hours, and ATRA + siRNA RAR-β also followed the same trend (Supplementary Fig. 7). qPCR analysis of control HSCs and 10-day ATRA-treated HSCs confirmed the shift towards quiescence as mRNA expression of both α-SMA and vimentin was significantly reduced (Fig. 5C). Oil Red O staining was performed to determine the presence of cytoplasmic lipid droplets (44). We confirmed that control activated HSCs showed minimal staining with Oil Red O, significantly less than observed in ATRA-treated HSCs (Fig. 5 D, E). Together, these results suggest the consistent acquisition of a quiescent phenotype of HSCs following ATRA treatment.

ATRA treatment reduces production of ECM proteins

One of the hallmarks of fibrosis is the deposition of excess levels of ECM proteins, such as collagen and fibronectin. Activated HSCs, in their role as stroma-resident stellate cells, secrete both collagen and fibronectin at high levels (3). The importance of fibronectin secretion in tumor microenvironments, and its transcriptional regulation in cancer, is substantiated by the specificity of alternatively spliced isoforms of fibronectin in different cancers. For example, liver cancer is associated with increased expression of the extra domain-A (EDA) spliced form of fibronectin (46), which can promote HSC motility (47). Another spliced form of fibronectin, extra domain-B (EDB), has been showed to promote fibroblast proliferation and deposition of fibronectin in mice (48).

Using qPCR, we observed that mRNA expression of fibronectin, fibronectin-EDA, fibronectin-EDB, and collagen I are significantly reduced following 10-day ATRA treatment (Fig. 6A), indicating the role of ATRA in inhibiting ECM protein transcription. At the protein level, immunofluorescence staining showed a significant reduction in both intracellular and extracellular fibronectin and collagen I in response to 10-day ATRA treatment. The presence of the RAR-β antagonist during the 10-day ATRA treatment reverted fibronectin and collagen I values to those observed in control HSCs. RAR-β agonist also significantly reduced expression of these ECM proteins, with rescue observed in combination with siRNA RAR-β (Fig. 6 B, C). 72 hour ATRA treatment also reduced expression, with rescued expression when combined with siRNA RAR-β (Supplementary Fig. 8). Collectively these results show that ATRA suppresses the transcription of collagen I and fibronectin, and their expression and secretion by HSCs.

ATRA inhibits durotaxis in HSCs

We have previously reported that HSCs can perform rigidity gradient directed movement towards a stiffer substrate, also known as durotaxis (19). We used a dual-rigidity gradient gel to determine whether ATRA can inhibit the ability of HSCs to exhibit durotaxis. The fibrotic microenvironment that facilitates tumor progression has increased rigidity compared to the rest of the stroma, and therefore durotaxis behaviour in HSCs represents a further mechanical positive-feedback loop by which HSCs accumulate in fibrotic areas and become activated to potentiate fibrosis.

We observed that control HSCs perform durotaxis as previously shown, travelling on average 73.5 μm towards the stiff substrate over 5.5 hours. Treatment of HSCs with either ATRA or the RAR-β agonist (cd2314) fully abrogated durotaxis behaviour, with no observable migration along the stiffness gradient. Durotaxis can be rescued in ATRA-treated cells with overexpression of MLC-2 (average distance travelled = 59.5 μm), indicating that ATRA exerts its effect by inhibiting myosin activity (Fig. 7A, C and videos 1-4). Correspondingly, cell speed (in all directions) is also affected by RAR-β activation, with control HSCs travelling on average 0.89 μm/min and RAR-β activation by ATRA and the RAR-β agonist significantly reducing this speed to 0.36 and 0.33 μm/min, respectively. As with durotaxis, MLC-2 overexpression could rescue the cell speed of ATRA treated cells to an average cell speed of 1.0 μm/min, a value not significantly different from the control condition (Fig. 7B). Together this indicates the sensitivity of durotaxis and cell migration to RAR-β signalling, providing further evidence for the manifold effects of retinoid signalling in a variety of cell behaviours that can regulate cancer development through mechanical positive feedback loops.

Discussion

Retinoids, metabolites of vitamin A, have long been studied in cancer therapeutics due to their varied effects on cells, with one of the most successful examples shown in the treatment of promyelocytic leukaemia (49). There exists a close link between RAR-β expression and cancer, with loss of the RAR-β2 isoform occurring in breast, lung, oesophagus, pancreas, cervix and prostate tumors (26). We report here that RAR-β expression is significantly reduced in both mouse models of fibrosis, and in human samples of cirrhosis and HCC. Interestingly, this loss of expression occurs in the tissue areas populated by HSCs. Therefore, our results corroborate the importance of RAR-β in cancer, and suggest that RAR-β might be an attractive target to develop new therapies against HSCs to suppress the desmoplastic reaction associated with HCC and cirrhosis.

As the primary cell type that drives liver fibrosis, HSCs are an important target in (i) understanding the emergence and maintenance of fibrosis, and (ii) developing therapeutics to abrogate the tumor permissive microenvironment (50). We show that MLC-2 expression *in vivo* increases with fibrosis, and also with the development of HCC through cirrhosis, and that RAR-β activation in our *in vitro* liver model, using liver specific substrate rigidity, downregulates MLC-2 expression. Negative regulation of MLC-2 *in vitro* inhibits cytoskeletal tension, endogenous forces, mechanosensing, and ECM deposition, the key components of the signalling loop that initiates and maintains the myofibroblast-like phenotype (24). Our results therefore reveal a previously unidentified mechanism to target mechanotransduction in HSCs by regulating MLC-2 transcription (Fig. 8), and we suggest that mechanical reprogramming of HSCs through RAR-β may be a plausible option for several liver disorders.

Cancer cells can recruit HSCs through secretion of cytokines that guide the migration of HSCs through chemotaxis (51). Mutually activating bidirectional crosstalk between hepatocytes and HSCs is known to promote a tumor permissive microenvironment and directed migration of HSCs to the tumor augments this crosstalk and HCC progression (11). We have recently shown that durotaxis is another mechanism by which HSCs can be recruited to the fibrotic site, with directed migration via a stiffness gradient (19). Furthermore, the stiff environment generated by activated HSCs can recruit yet more HSCs through durotaxis, leading to accumulation (50). Durotaxis therefore represents a cellular process that underpins multiple positive feedback loops. Notably, we observe that ATRA inhibits HSC durotaxis through downregulation of MLC-2 expression and subsequent mechanical deactivation, which implies that retinoid

signalling can reduce inter-cell pro-oncogenic crosstalk, both between cancer cells and HSCs, and within the wider HSC population.

The potential therapeutic value of mechanical deactivation of HSCs through the RAR-β/ MLC-2 axis is not limited to HCC, as stromal remodelling by HSCs and other myofibroblast-like cells is essential in the progression of other diseases with a wider impact on the worldwide population, such as non-alcoholic fatty liver disease (NAFLD). In NAFLD mouse models, a synthetic agonist of RAR-β has been shown to deactivate HSCs, leading to reduced steatosis and oxidative stress in the liver (52). It has been documented that fibrosis in NAFLD is reversible (53), and our observation that RAR-β activation prevents stromal remodelling by HSCs, when viewed in conjunction with the previous studies on NAFLD mouse models, emphasises the importance of retinoid signalling in HSCs and its wide ranging therapeutic potential.

Furthermore, it is known that PDAC cells form metastases in the liver preceding formation of the primary tumor (54). Colonising PDAC cells require a pre-metastatic niche in the liver, with the activation of HSCs, and subsequent increased fibronectin deposition, indispensable for the formation of this niche (12). Therefore, we propose that RAR-β may be also relevant for clinical intervention of PDAC metastasis in the liver.

Our combined findings highlight RAR-β as a transcriptional regulator of cell biomechanics and microenvironmental remodelling in HSCs. The increasing but still emerging appreciation that mechanotransduction is fundamental in the biology of stromal cells such as HSCs should lead to innovative approaches in stromal reprogramming and reversal of several liver disorders.

References

1. Pinter M, Trauner M, Peck-Radosavljevic M, Sieghart W. Cancer and liver cirrhosis: implications on prognosis and management. ESMO Open 2016;1:e000042.
2. Sakurai T, Kudo M. Molecular Link between Liver Fibrosis and Hepatocellular Carcinoma. Liver Cancer 2013;2:365-366.
3. Bataller R, Brenner DA. Liver fibrosis. J Clin Invest 2005;115:209-218.
4. Luedde T, Schwabe RF. NF-kappaB in the liver--linking injury, fibrosis and hepatocellular carcinoma. Nat Rev Gastroenterol Hepatol 2011;8:108-118.
5. Benedict M, Zhang X. Non-alcoholic fatty liver disease: An expanded review. World J Hepatol 2017;9:715-732.
6. Wobser H, Dorn C, Weiss TS, Amann T, Bollheimer C, Buttner R, Scholmerich J, et al. Lipid accumulation in hepatocytes induces fibrogenic activation of hepatic stellate cells. Cell Res 2009;19:996-1005.
7. Moreira RK. Hepatic stellate cells and liver fibrosis. Arch Pathol Lab Med 2007;131:1728-1734.
8. Puche JE, Saiman Y, Friedman SL. Hepatic stellate cells and liver fibrosis. Compr Physiol 2013;3:1473-1492.
9. Carloni V, Luong TV, Rombouts K. Hepatic stellate cells and extracellular matrix in hepatocellular carcinoma: more complicated than ever. Liver Int 2014;34:834-843.
10. Tsuchida T, Friedman SL. Mechanisms of hepatic stellate cell activation. Nat Rev Gastroenterol Hepatol 2017;14:397-411.
11. Coulouarn C, Corlu A, Glaise D, Guenon I, Thorgeirsson SS, Clement B. Hepatocyte-stellate cell cross-talk in the liver engenders a permissive inflammatory microenvironment that drives progression in hepatocellular carcinoma. Cancer Res 2012;72:2533-2542.

12. Costa-Silva B, Aiello NM, Ocean AJ, Singh S, Zhang H, Thakur BK, Becker A, et al. Pancreatic cancer exosomes initiate pre-metastatic niche formation in the liver. Nat Cell Biol 2015;17:816-826.
13. Omary MB, Lugea A, Lowe AW, Pandol SJ. The pancreatic stellate cell: a star on the rise in pancreatic diseases. J Clin Invest 2007;117:50-59.
14. Jaster R. Molecular regulation of pancreatic stellate cell function. Mol Cancer 2004;3:26.
15. Cirri P, Chiarugi P. Cancer associated fibroblasts: the dark side of the coin. Am J Cancer Res 2011;1:482-497.
16. Lachowski D, Cortes E, Pink D, Chronopoulos A, Karim SA, J PM, Del Rio Hernandez AE. Substrate Rigidity Controls Activation and Durotaxis in Pancreatic Stellate Cells. Sci Rep 2017;7:2506.
17. Calvo F, Ege N, Grande-Garcia A, Hooper S, Jenkins RP, Chaudhry SI, Harrington K, et al. Mechanotransduction and YAP-dependent matrix remodelling is required for the generation and maintenance of cancer-associated fibroblasts. Nat Cell Biol 2013;15:637-646.
18. Amann T, Bataille F, Spruss T, Muhlbauer M, Gabele E, Scholmerich J, Kiefer P, et al. Activated hepatic stellate cells promote tumorigenicity of hepatocellular carcinoma. Cancer Sci 2009;100:646-653.
19. Lachowski D, Cortes E, Robinson B, Rice A, Rombouts K, Del Rio Hernandez AE. FAK controls the mechanical activation of YAP, a transcriptional regulator required for durotaxis. FASEB J 2017.
20. Pinato DJ, Black JR, Trousil S, Dina RE, Trivedi P, Mauri FA, Sharma R. Programmed cell death ligands expression in phaeochromocytomas and paragangliomas: Relationship with the hypoxic response, immune evasion and malignant behavior. Oncoimmunology 2017;6:e1358332.
21. Li B, Ruotti V, Stewart RM, Thomson JA, Dewey CN. RNA-Seq gene expression estimation with read mapping uncertainty. Bioinformatics 2010;26:493-500.
22. Love MI, Huber W, Anders S. Moderated estimation of fold change and dispersion for RNA-seq data with DESeq2. Genome Biol 2014;15:550.
23. Harris AR, Charras GT. Experimental validation of atomic force microscopy-based cell elasticity measurements. Nanotechnology 2011;22:345102.
24. Hellemans K, Verbuyst P, Quartier E, Schuit F, Rombouts K, Chandraratna RA, Schuppan D, et al. Differential modulation of rat hepatic stellate phenotype by natural and synthetic retinoids. Hepatology 2004;39:97-108.
25. Ohata M, Lin M, Satre M, Tsukamoto H. Diminished retinoic acid signaling in hepatic stellate cells in cholestatic liver fibrosis. Am J Physiol 1997;272:G589-596.
26. Xu XC. Tumor-suppressive activity of retinoic acid receptor-beta in cancer. Cancer Lett 2007;253:14-24.
27. Blomhoff R, Blomhoff HK. Overview of retinoid metabolism and function. J Neurobiol 2006;66:606-630.
28. Takeyama K, Kojima R, Ohashi R, Sato T, Mano H, Masushige S, Kato S. Retinoic acid differentially up-regulates the gene expression of retinoic acid receptor alpha and gamma isoforms in embryo and adult rats. Biochem Biophys Res Commun 1996;222:395-400.
29. Takami Y, Yamamoto I, Tsubouchi H, Gohda E. Modulation of hepatocyte growth factor induction in human skin fibroblasts by retinoic acid. Biochim Biophys Acta 2005;1743:49-56.
30. Chronopoulos A, Robinson B, Sarper M, Cortes E, Auernheimer V, Lachowski D, Attwood S, et al. ATRA mechanically reprograms pancreatic stellate cells to suppress matrix remodelling and inhibit cancer cell invasion. Nat Commun 2016;7:12630.

31. Sarper M, Cortes E, Lieberthal TJ, Del Rio Hernandez A. ATRA modulates mechanical activation of TGF-beta by pancreatic stellate cells. Sci Rep 2016;6:27639.
32. Zhubanchaliyev A, Temirbekuly A, Kongrtay K, Wanshura LC, Kunz J. Targeting Mechanotransduction at the Transcriptional Level: YAP and BRD4 Are Novel Therapeutic Targets for the Reversal of Liver Fibrosis. Front Pharmacol 2016;7:462.
33. Zaidel-Bar R, Zhenhuan G, Luxenburg C. The contractome--a systems view of actomyosin contractility in non-muscle cells. J Cell Sci 2015;128:2209-2217.
34. Scholten D, Trebicka J, Liedtke C, Weiskirchen R. The carbon tetrachloride model in mice. Lab Anim 2015;49:4-11.
35. Edge SB, Compton CC. The American Joint Committee on Cancer: the 7th edition of the AJCC cancer staging manual and the future of TNM. Ann Surg Oncol 2010;17:1471-1474.
36. Mueller S, Sandrin L. Liver stiffness: a novel parameter for the diagnosis of liver disease. Hepatic Medicine: Evidence and Researcj 2010;2:49-67.
37. Bataller R, Nicolas JM, Ginees P, Gorbig MN, Garcia-Ramallo E, Lario S, Tobias E, et al. Contraction of human hepatic stellate cells activated in culture: a role for voltage-operated calcium channels. J Hepatol 1998;29:398-408.
38. Stamenovic D. Effects of cytoskeletal prestress on cell rheological behavior. Acta Biomater 2005;1:255-262.
39. Wang N, Tolic-Norrelykke IM, Chen J, Mijailovich SM, Butler JP, Fredberg JJ, Stamenovic D. Cell prestress. I. Stiffness and prestress are closely associated in adherent contractile cells. Am J Physiol Cell Physiol 2002;282:C606-616.
40. Kuznetsova TG, Starodubtseva MN, Yegorenkov NI, Chizhik SA, Zhdanov RI. Atomic force microscopy probing of cell elasticity. Micron 2007;38:824-833.
41. Cui X, Zhang X, Yin Q, Meng A, Su S, Jing X, Li H, et al. Factin cytoskeleton reorganization is associated with hepatic stellate cell activation. Mol Med Rep 2014;9:1641-1647.
42. Guilluy C, Swaminathan V, Garcia-Mata R, O'Brien ET, Superfine R, Burridge K. The Rho GEFs LARG and GEF-H1 regulate the mechanical response to force on integrins. Nat Cell Biol 2011;13:722-727.
43. Ho YY, Lagares D, Tager AM, Kapoor M. Fibrosis--a lethal component of systemic sclerosis. Nat Rev Rheumatol 2014;10:390-402.
44. Jesnowski R, Furst D, Ringel J, Chen Y, Schrodel A, Kleeff J, Kolb A, et al. Immortalization of pancreatic stellate cells as an in vitro model of pancreatic fibrosis: deactivation is induced by matrigel and N-acetylcysteine. Lab Invest 2005;85:1276-1291.
45. Liu CY, Lin HH, Tang MJ, Wang YK. Vimentin contributes to epithelial-mesenchymal transition cancer cell mechanics by mediating cytoskeletal organization and focal adhesion maturation. Oncotarget 2015;6:15966-15983.
46. Rybak JN, Roesli C, Kaspar M, Villa A, Neri D. The extra-domain A of fibronectin is a vascular marker of solid tumors and metastases. Cancer Res 2007;67:10948-10957.
47. Olsen AL, Sackey BK, Marcinkiewicz C, Boettiger D, Wells RG. Fibronectin extra domain-A promotes hepatic stellate cell motility but not differentiation into myofibroblasts. Gastroenterology 2012;142:928-937 e923.
48. Fukuda T, Yoshida N, Kataoka Y, Manabe R, Mizuno-Horikawa Y, Sato M, Kuriyama K, et al. Mice lacking the EDB segment of fibronectin develop normally but exhibit reduced cell growth and fibronectin matrix assembly in vitro. Cancer Res 2002;62:5603-5610.
49. Ablain J, de The H. Retinoic acid signaling in cancer: The parable of acute promyelocytic leukemia. Int J Cancer 2014;135:2262-2272.
50. Wells RG. The role of matrix stiffness in hepatic stellate cell activation and liver fibrosis. J Clin Gastroenterol 2005;39:S158-161.

51. Yang C, Zeisberg M, Mosterman B, Sudhakar A, Yerramalla U, Holthaus K, Xu L, et al. Liver fibrosis: insights into migration of hepatic stellate cells in response to extracellular matrix and growth factors. Gastroenterology 2003;124:147-159.
52. Trasino SE, Tang XH, Jessurun J, Gudas LJ. A retinoic acid receptor beta2 agonist reduces hepatic stellate cell activation in nonalcoholic fatty liver disease. J Mol Med (Berl) 2016;94:1143-1151.
53. Ellis EL, Mann DA. Clinical evidence for the regression of liver fibrosis. J Hepatol 2012;56:1171-1180.
54. Rhim AD, Mirek ET, Aiello NM, Maitra A, Bailey JM, McAllister F, Reichert M, et al. EMT and dissemination precede pancreatic tumor formation. Cell 2012;148:349-361.

Acknowledgements
The authors thank the Cellular and Molecular Biomechanics Laboratory members for help and advice throughout this work. DJP acknowledges support from the National Institute for Health Research (NIHR) as well as infrastructural support from the Imperial Experimental Cancer Medicine Centre, Cancer Research UK Imperial Centre the Imperial Biomedical Research Centre (BRC) and the Imperial College Tissue Bank.

Author contributions
EC and ADRH conceived the idea and designed research. EC, DL, AR, AC, BR performed experimental research and analysed data under the supervision of ADRH. HW analysed mRNA data for RAR-β expression from the TCGA. DJP provided the TMA. LAP provided murine tissues. EC, AR, and ADRH wrote the paper.

Conflict of interest
The authors declare no conflict of interest

Figure legends:
Figure 1. **RAR-β is downregulated in activated HSCs and all trans-retinoic acid (ATRA) activates RAR-β expression in HSCs**. **(A)** Immunofluorescence images of healthy and cirrhotic liver human tissues, scale bar = 100 μm. 10 patients per condition and more than 8 sections per patients. **(B)** Quantification of RAR-β expression in healthy and cirrhotic tissues. **(C)** Quantification of RAR-β expression in tissues from normal and HCC patients. **(D)** qPCR levels of RAR-β in HSCs, normalized to GAPDH and relative to control. **(E)** Quantification of RAR-β staining in HSCs. **(F)** Representative images for immunofluorescence staining of HSCs, scale bar = 20 μm (left) and western blot bands for protein expression in HSCs (right)All histogram bars represent mean ± s.e.m., **P<0.01,***P<0.001. T-test. Three experimental replicates in all panels.

Figure 2. ATRA downregulates expression and activation of MLC-2 in HSCs via RAR-β **(A)** qPCR levels of MLC-2 in HSCs, normalized to GAPDH and relative to control**. (B)** Quantification of MLC-2 and pMLC-2 staining in HSCs. **(C)** Representative images of MLC-2 and pMLC-2 staining, scale bar = 20 μm. (D) Representative images of tissue immunostaining for murine livers (vehicle control and CCl4-induced fibrosis), scale bar is 50 μm (left) and quantification of immunofluorescence staining (right), number of mice: 5 CCl_4-induced fibrosis and 3 controls. All histogram bars represent mean±sem,**P<0.01,***P<0.001. Three experimental replicates in all panels. Anova and Tukey's post hoc test for A and B and t-test for D.

Figure 3. (A) Representative images of human tissue immunostaining for healthy, cirrhotic, and HCC (hepatocellular carcinoma) livers, scale bar is 50 μm. **(B)** Quantification of immunofluorescence staining for panel A (number of patients: 10 healthy, 22 cirrhosis, and 48 HCC. **(C)** Correlation of RAR-β and MLC-2 expression in human HCC liver tissues. HCC tissues were classified and divided in two groups according to the TNM stage (20 T1/T2 and 25 T3/T4 patients). **(D)** Representative images of immunofluorescence staining of HSCs seeded in 12 kPa PAA (polyacrylamide gels). The yellow arrow indicates the nuclear localization of RAR-β in the ATRA treated HSCs, scale bar is 20 μm. **(E)** Quantification of fluorescence intensity for images in panel D. Histogram bars represent mean ± sem,*P<0.05, **P<0.01,***P<0.001 (t-test).

Figure 4. ATRA suppresses force generation, gel contraction, and mechanosensing by HSCs.
(A) Heat maps representing forces applied by HSCs on top of the pillars, scale bar 20 μm. **(B)** Quantification of average forces applied by HSCs on pillars. For control, ATRA, ATRA + RAR β antagonist, RAR β agonist, siRNA RAR β + RAR β agonist, n = 50,37,50,39,49 cells respectively. Mann-Whitney test for significance, ***P < 0.001 **(C)** Quantification of cell compliance with atomic force microscopy. Cantilevers used had a 15 μm diameter polystyrene bead attached. For control and ATRA, n = 60,44,27,25,21 cells respectively. Mann-Whitney test for significance, *P < 0.05 **(D)** Left: Quantification of contraction of gels embedded with HSCs, each dot representing a gel. Anova and Tukey's post hoc test, ***p < 0.001. Right: Representative images of gel contraction (Y27632 is an inhibitor of MLC-2 activation and cell contractility. Discontinuous yellow lines mark the gel contours. **(E)** Schematic of the methodology to test mechanosensing using magnetic tweezers. **(F)** Left: Representative trace that shows the decrease in the amplitude of oscillation of a bead attached to a cell that can sense external mechanical stimuli (mechanosensing). Right: Histogram shows relative bead displacement for the first and last pulse, n=16 for control and ATRA. Mann-Whitney test for significance, **P<0.01

Figure 5. ATRA induces a quiescent morphology in HSCs.
(A) Immunofluorescence images for the alpha smooth muscle actin - α–SMA and vimentin (markers for myofibroblast phenotype), scale bar is 20μm. **(B)** Quantification of the stained HSCs after treatment. The intensity of the staining was calculated by measuring Mean Fluorescent Intensity (MFI) of cell area by ImageJ.. **(C)** qPCR levels of αSMA and vimentin in HSCs, normalized to GAPDH and relative to control**. (D)** Representative images for Oil Red O staining of HSCs, scale bar is 10 μm. **(E)** Quantification of Oil Red O staining, each dot represents a field of view. Histogram bars represent mean mean ± s.e.m. **, p<0.01; ***, p<0.001 (t-test). Three experimental replicates in all panels.

Figure 6. ATRA inhibits synthesis and secretion of fibronectin (FN) and collagen I by HSC. (A) qPCR levels of ECM proteins in HSCs, normalized to GAPDH and relative to control. Fibronectin extracellular domain A (FN-EDA), fibronectin extracellular domain B (FN-EDB),**. (B)** Representative images for immunofluorescence staining of HSCs, scale bar 20 μm. **(C)** Quantification of fibronectin (FN), and collagen I staining in HSCs. Histogram bars represent mean ± s.e.m. *, p<0.05; **, p<0.01; ***, p<0.001 (Anova and Tukey's post hoc test). Three experimental replicates.

Figure 7. ATRA inhibits durotaxis in HSCs. (A) Average cell movement distance on the soft-stiff rigidity gradient compared to single rigidity soft and stiff substrates presented as an average displacement (positive values indicate directed movement towards stiff substrate,

negative values towards soft substrate and 0 indicates random movement). n = 3 independent experiments. Results are expressed as mean ± s.e.m. **(B)** Cell movement speed on the soft-stiff rigidity gradient compared to single rigidity soft and stiff substrates. Results are expressed as mean ± s.e.m. **(C)** Representation of the average displacements of HSCs. Quantification was done for 60 cells. Three experimental replicates in all cases. Results are expressed as mean ± sem. Anova and Tukey's post hoc tests were used for the analysis.

Figure 8. Model illustrating the effect of RAR-β activation in HSCs.

Figure 1 Manuscript: HEP-18-492

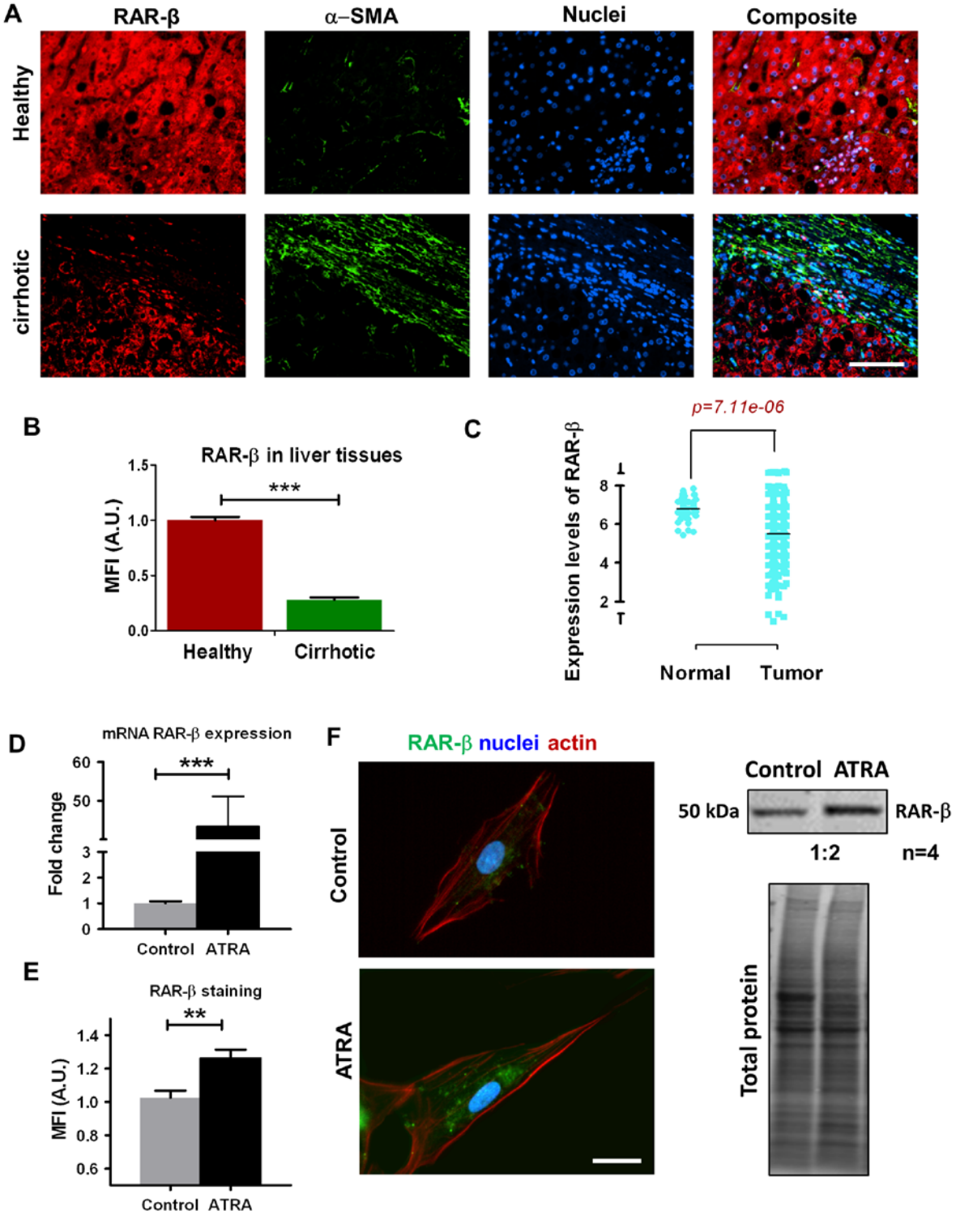

Figure 2 Manuscript: HEP-18-492

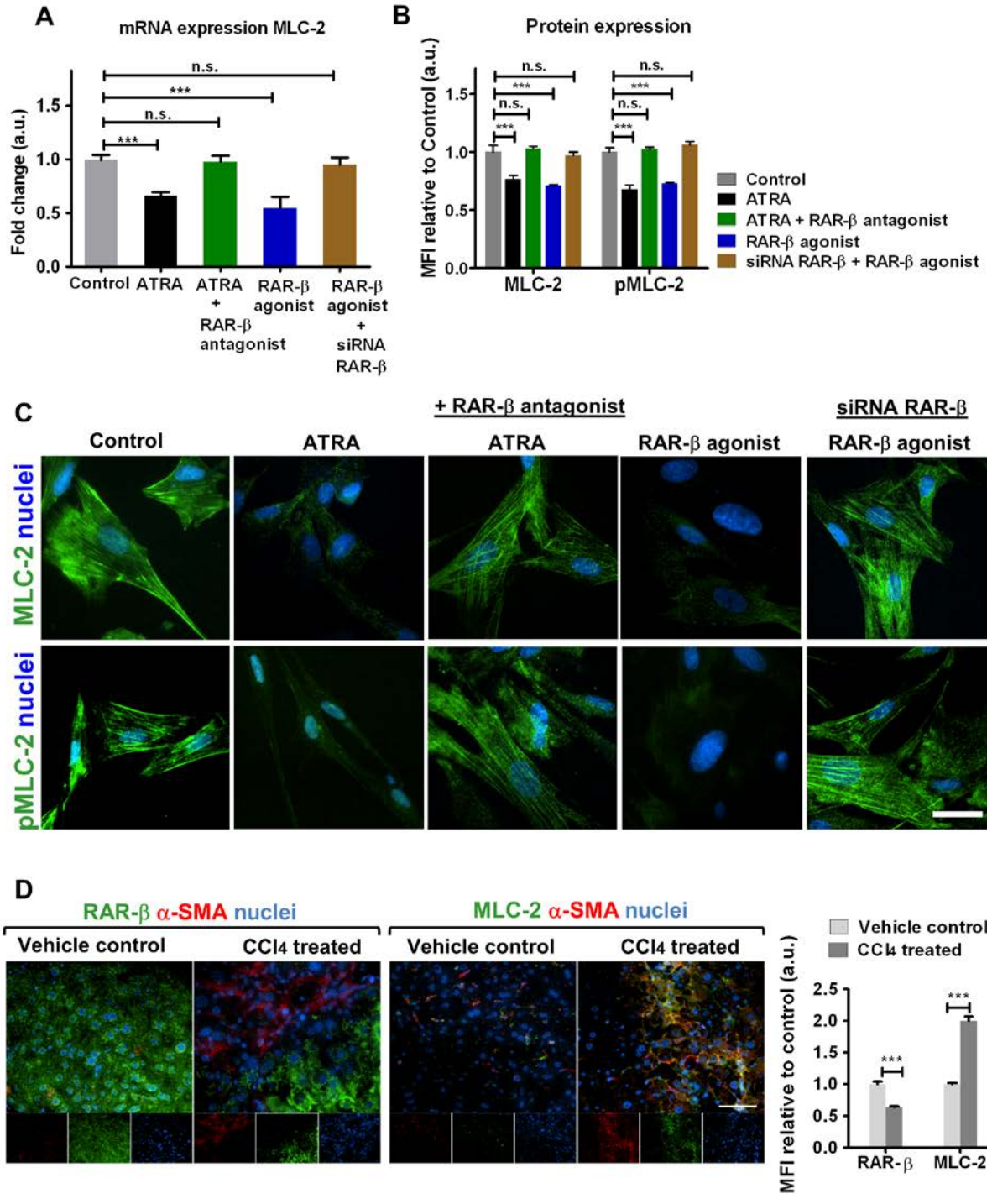

Figure 3 Manuscript: HEP-18-492

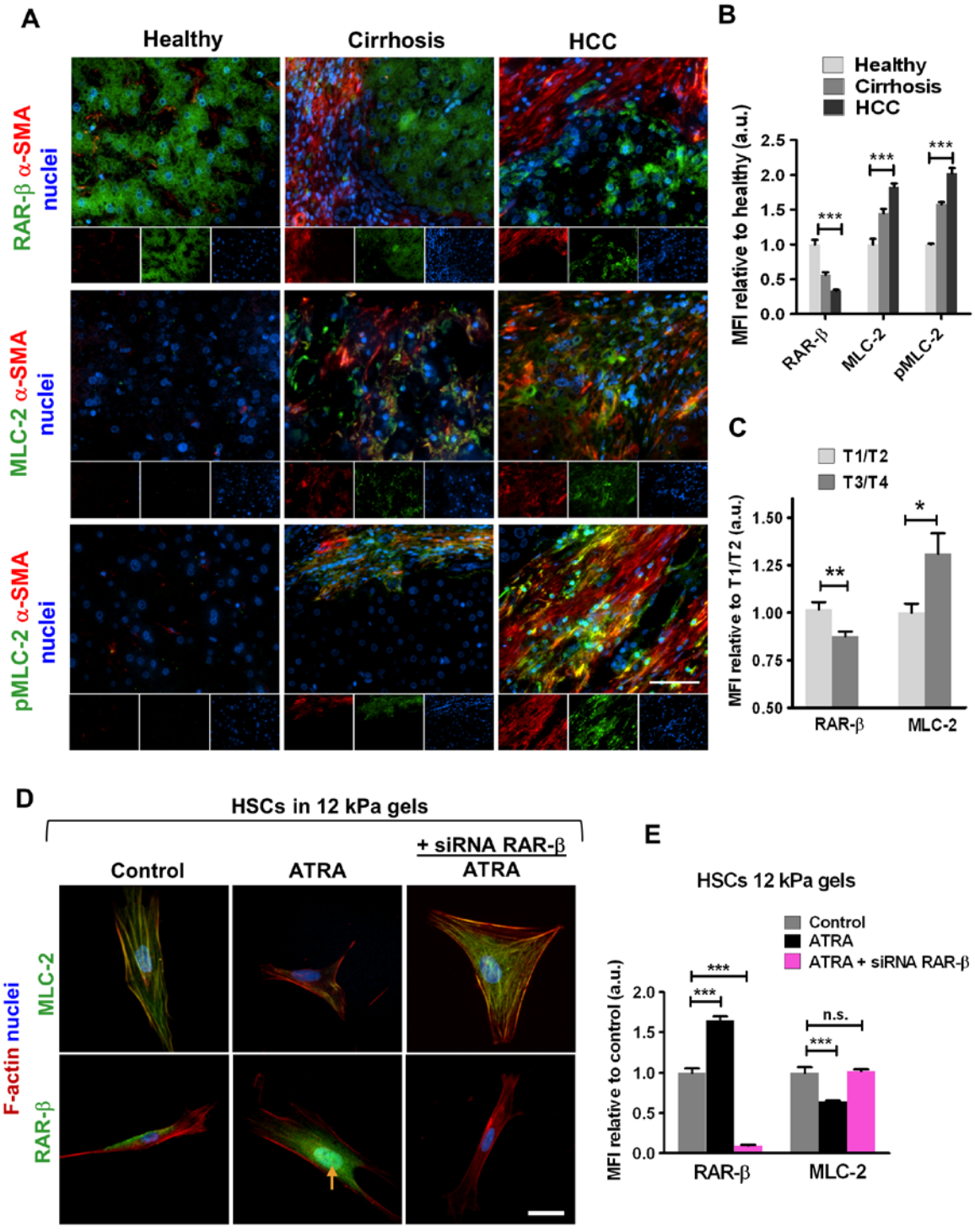

Figure 4 Manuscript: HEP-18-492

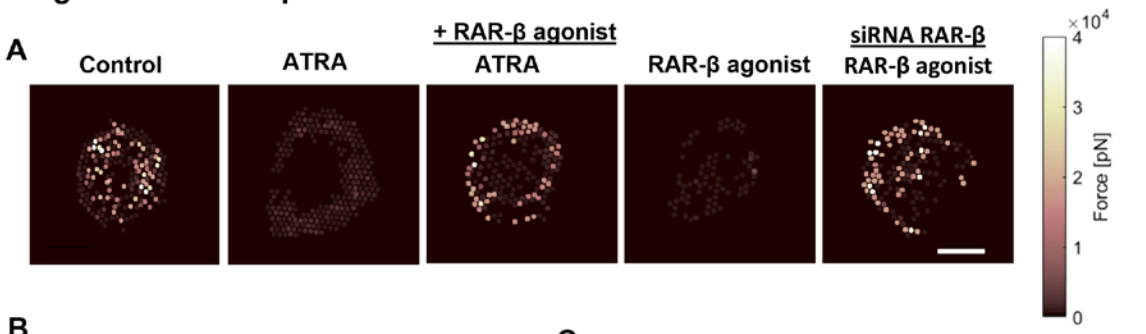

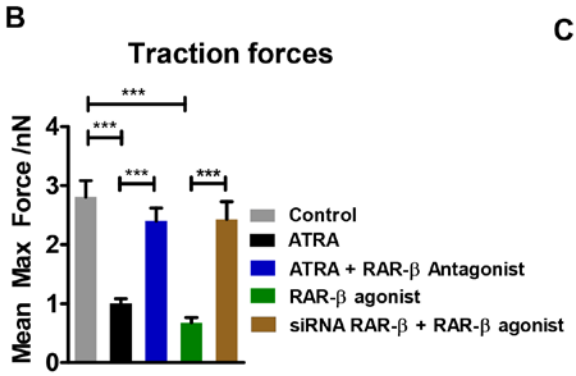

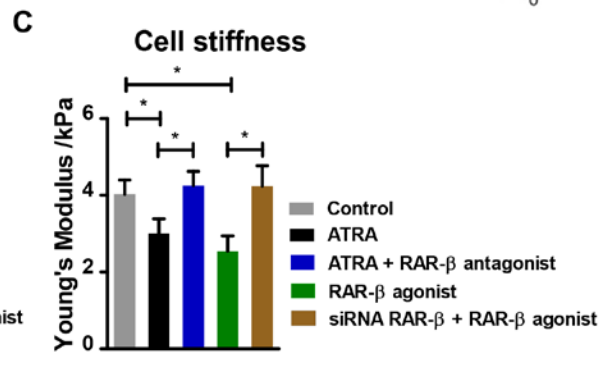

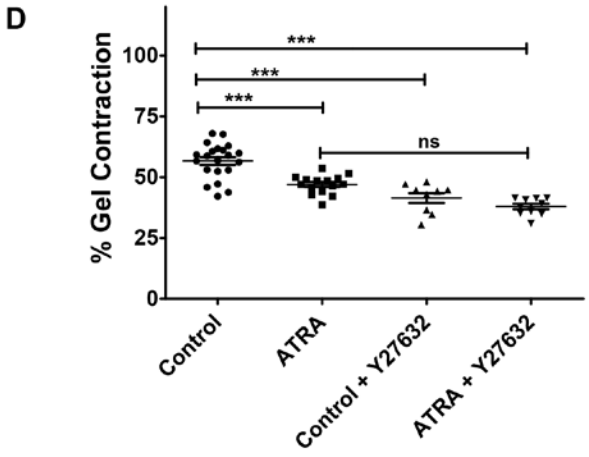

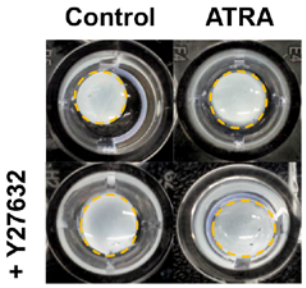

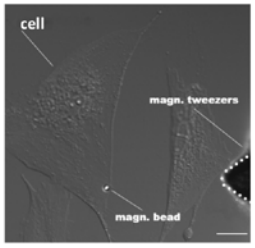

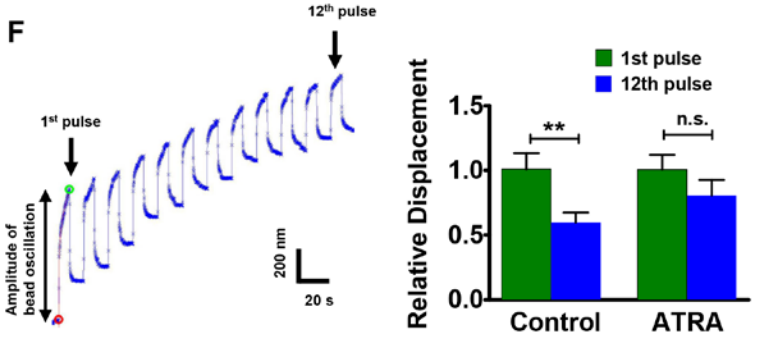

Figure 5 Manuscript: HEP-18-492

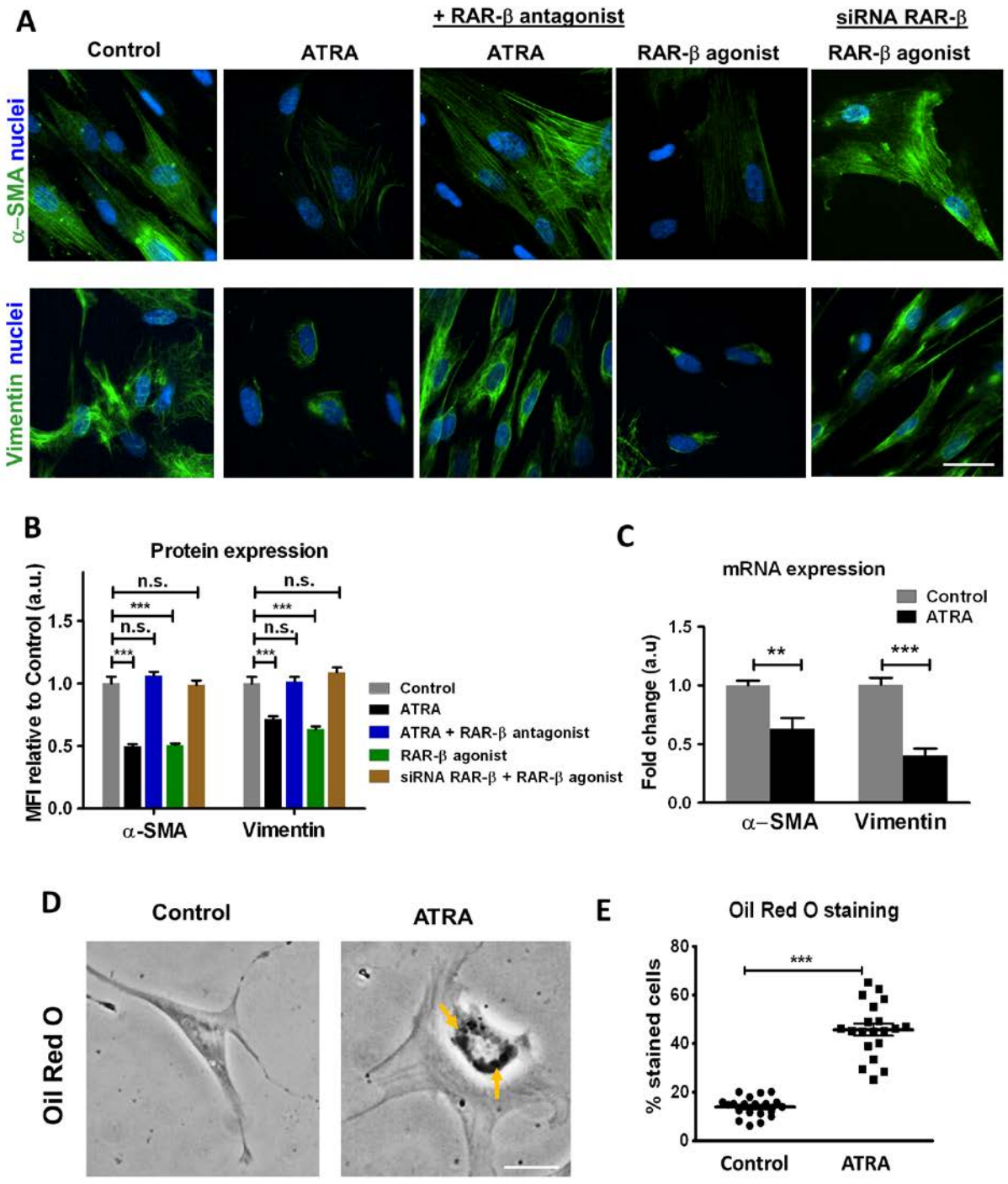

Figure 6 Manuscript: HEP-18-492

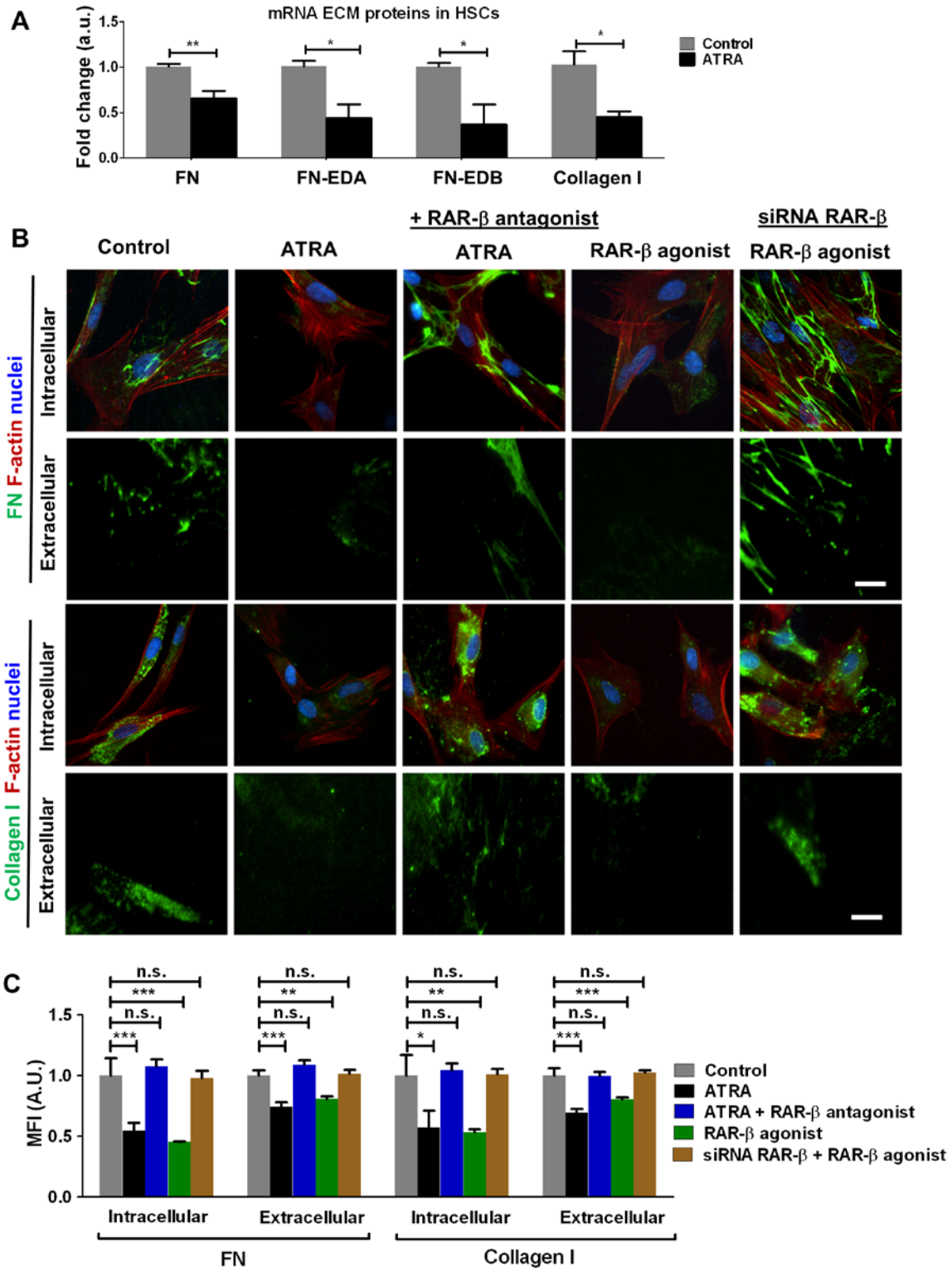

Figure 7 Manuscript: HEP-18-492

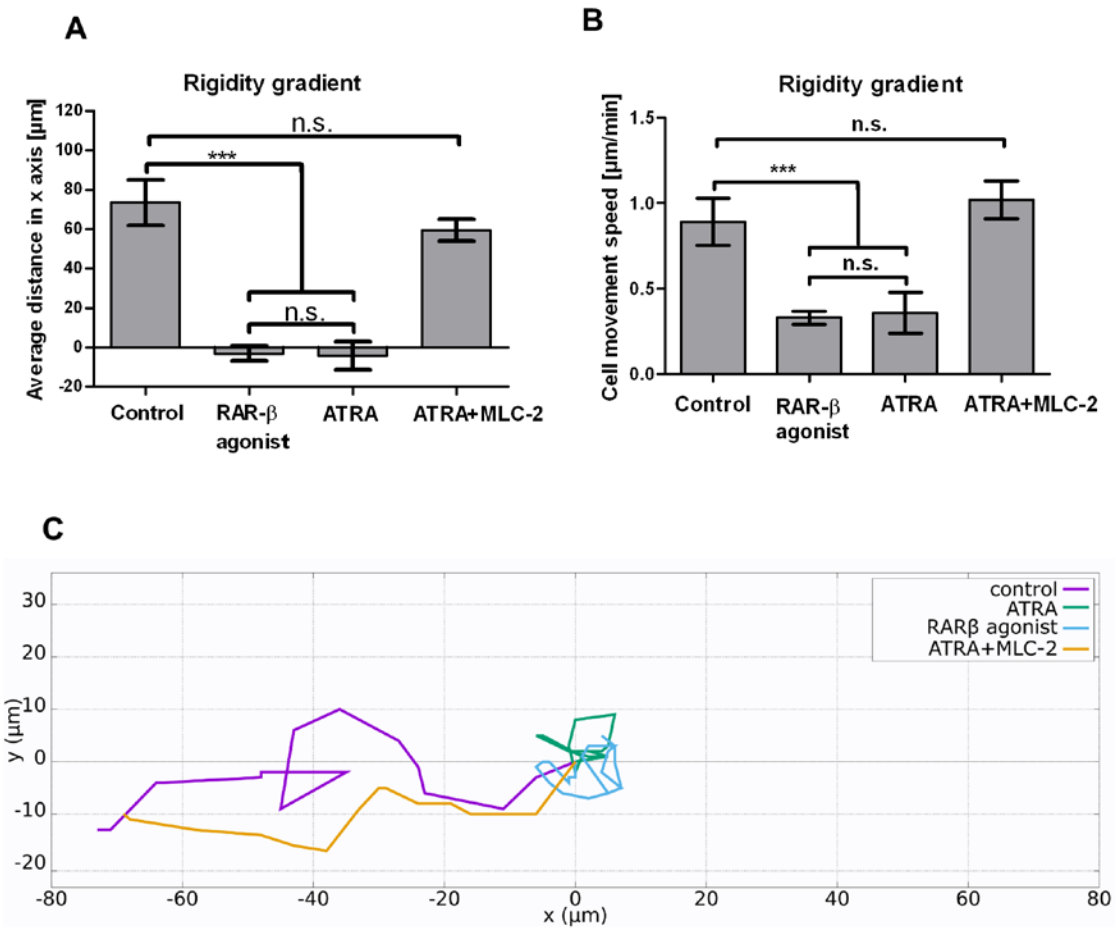

Figure 8 Manuscript: HEP-18-492